Journal of Sound and Vibration 510 (2021) 116295

Contents lists available at ScienceDirect

Journal of Sound and Vibration

journal homepage: www.elsevier.com/locate/jsvi

Three-dimensional nonlinear extreme vibrations of cantilevers based on a geometrically exact model

Hamed Farokhi [a,*], Alper Erturk [b]

[a] Department of Mechanical and Construction Engineering, Northumbria University, Newcastle upon, Tyne NE1 8ST, UK
[b] George W. Woodruff School of Mechanical Engineering, Georgia Institute of Technology, Atlanta, 30332, USA

ARTICLE INFO

Keywords:
Three-dimensional motion
Geometrically exact model
Nonlinear dynamics
Large-amplitude vibrations

ABSTRACT

In this paper, a three-dimensional geometrically exact model is developed for cantilevers, for the first time, which allows for accurate analysis of oscillations of extremely large amplitude. The proposed exact model is on the basis of three Euler angles describing the centreline motion. Euler–Bernoulli beam theory is utilised together with Kelvin–Voigt material damping, while utilising the centreline-inextensibility assumption. Hamilton's principle is utilised to derive the equations of motion for the three rotational motions, while keeping all terms geometrically exact. Galerkin discretisation is performed on the three partial differential equations of motion and the resultant set of discretised equations is solved using a continuation technique. The unique feature of the proposed exact model is its capability to capture very large-amplitude vibrations accurately, for both two-dimensional and three-dimensional motions. The dynamical response of the cantilever is examined in detail in the primary resonance region, highlighting the effect of the one-to-one internal resonance between the in-plane and out-of-plane transverse motions. A comparison between the geometrically exact model and the third-order nonlinear model is conducted to better showcase the significance of the proposed exact model, and the limitations of a truncated third-order model.

1. Introduction

Beam, plate, and shell structures can be found in various engineering systems [1–8]. As a sub-class of these structures, cantilevers are present in numerous engineering applications ranging from macro [2,9,10] to nano scale, such as micro/nano-electromechanical systems, micro gyroscopes, vibration energy harvesters, and scanning probe microscopy [11–16]. Due to having one end free, cantilevers could undergo large-amplitude oscillations under relatively small base excitation magnitudes. In fact, the capability to undergo large-amplitude oscillations is very desirable in certain applications such as in inverted-flag-based flow energy harvesters [17–19]. However, accurate prediction of the response of a cantilever undergoing oscillations of very large amplitudes is a difficult task due to presence of various sources of nonlinearity, such as geometric nonlinearities due to large rotations as well as inertial nonlinearities arising from centreline inextensibility. A concise review of the literature is given in the following, focusing on the key models developed to date and highlighting the limitations of the currently available models in the literature.

Examining the dynamical behaviour of cantilevers has been the subject of investigation by many researchers over the last few decades. Most of these studies examine the planar, i.e. two-dimensional (2D), dynamics of cantilevers while some examine their three-dimensional (3D) motion. One of the early investigations on 3D dynamics of cantilevers was conducted by Crespo da Silva and Glynn [20,21], who derived the inextensional equations governing the motion of cantilevers taking into account geometric and inertial nonlinearities; they utilised the method of multiple scales to study the cantilever dynamics. Nayfeh and Pai [22,23]

* Corresponding author.
E-mail address: hamed.farokhi@northumbria.ac.uk (H. Farokhi).

https://doi.org/10.1016/j.jsv.2021.116295
Received 16 March 2021; Received in revised form 9 June 2021; Accepted 13 June 2021
Available online 18 June 2021
0022-460X/© 2021 Elsevier Ltd. All rights reserved.

continued the investigations on dynamics of cantilevers by examining the 2D transverse vibration of cantilevers under transverse and axial base excitations; they utilised the inextensibility assumption to derive the nonlinear third-order equation of motion and used the method multiple scales together with the Galerkin scheme to solve the equation of motion. Further investigations were carried out by Hsieh et al. [24], who utilised an invariant manifold method to obtain the nonlinear normal vibration modes for finite amplitude response of a cantilever, and realised that the mode shapes of a linear cantilever can be effectively used for describing the nonlinear mode shapes. Further studies on this topic were performed by Feng and Leal [25], Anderson et al. [26], and Oh and Nayfeh [27], focusing on the symmetries in an inextensible cantilever beam equations, vibration of a parametrically excited cantilever, and presence of combination resonances in composite cantilever plates, respectively.

The investigations on nonlinear two dimensional dynamics of cantilevered beams were continued by Herişanu and Marinca [28], who proposed an analytical approximation for the nonlinear transverse free vibrations making use of the inextensibility assumption. In a recent study, Farokhi et al. [29] developed a two-dimensional geometrically exact nonlinear model for a cantilever capable of examining in-plane vibrations of extreme amplitudes. Cantilevered beam models have also been used in many other investigations, including those on piezoelectrically actuated beams, mass sensors, and vibration energy harvesters [30–37].

Furthermore, the unified theory of beams including geometrical nonlinearities, and specifically the Carrera Unified Formulation (CUF) [38], have also been used to study extremely large deflections of cantilevered beams with different cross-sections. The CUF can be utilised to implement high order 1D finite elements along the thickness direction; as a result of this, the mathematical model's accuracy becomes independent of the finite element discretisation and is tuned via increasing the theory approximation order. Pagani and Carrera [39] utilised the CUF and a total Lagrangian approach to introduce a unified beam theory with geometric nonlinearities, and used this formulation to analyse large deflection, buckling, and postbuckling of solid cross-section beams as well as thin-walled structures. Pagani et al. [40] examined the frequency and mode change in post-buckled thin-walled beams and those undergoing large deflections. The investigations were further continued by Carrera et al. [41,42] who examined the nonlinear large-amplitude response of beams with highly-deformable cross-sections and studied the frequency and mode change of thin-walled shell structures subject to large displacements and rotations.

The objective of the present study is to develop a three-dimensional (3D) geometrically exact analytical model for a cantilever for analysing in-plane and out-of-plane vibrations of extremely large amplitude. To the authors' best knowledge, such a model has not been developed to date. This study, for the first time, proposes a 3D exact model for a cantilever based on the three Euler angles. The unique feature of the proposed model is that the equations of motion are obtained for the three centreline rotation angles, rather than the centreline displacements, and all terms are kept intact (hence the geometrically exact model). The only 3D beam models developed for cantilevers to date are those proposed initially by Crespo da Silva and Glynn [20,21] and then by Nayfeh and co-workers [43,44]. These nonlinear 3D models are based on truncation of geometrically nonlinear terms up to cubic order, and hence they work well only for moderately large oscillations (refer to Section for 7 for a detailed comparison). The proposed exact model, however, is capable of examining oscillations of extremely large amplitudes in both two-dimensional (2D) and three-dimensional regimes. The accuracy of the proposed model is verified for the case of 2D motion via comparison to a 2D exact model [29], and for the case of 3D motion via comparison to a 3D nonlinear finite element model. Additionally, thorough comparisons are conducted between the proposed 3D exact model and the 3D third-order nonlinear model of the cantilever to better highlight the limitations of the truncated model. The nonlinear extreme dynamics of the cantilever is examined in primary resonance region, showcasing various bifurcation points and transitions from 2D to 3D motion.

2. Analytical model development

In this section, the three-dimensional geometrically exact nonlinear model for a homogeneous cantilevered beam is derived in detail while assuming an inextensible centreline. The system under consideration is a cantilevered beam of length L, mass per unit length m, Young's modulus E, material damping η, shear modulus G, and cross-sectional area A. The coordinate system associated with the undeformed geometry is denoted by xyz, while the curvilinear coordinate s indicates the distance of any points on the cantilever from the clamped end. The cantilever is under harmonic base excitation of $y_0 \sin(\omega_y t)$ in the y direction.

The motion of the cantilever from the undeformed to deformed state is described via three consecutive Euler angles, namely ψ, θ, and φ, as shown for a differential element in Fig. 1. In what follows, the equations of motion of the cantilever are obtained for these three angles while keeping all the terms geometrically exact. These equations allow for accurate analysis of the nonlinear oscillations of very large amplitudes, even when the tip angle grows larger than $\pi/2$.

Denoting the centreline strain by e and the displacements in the x, y, and z directions by u, v, and w, respectively, the following expressions for ψ and θ can be obtained based on Fig. 1 [43]

$$\begin{aligned}
\sin\psi(s,t) &= \frac{\partial_s v(s,t)}{\sqrt{\left(1+\partial_s u(s,t)\right)^2+\left(\partial_s v(s,t)\right)^2}},\\
\cos\psi(s,t) &= \frac{1+\partial_s u(s,t)}{\sqrt{\left(1+\partial_s u(s,t)\right)^2+\left(\partial_s v(s,t)\right)^2}},\\
\sin\theta(s,t) &= \frac{-\partial_s w(s,t)}{1+e},\\
\cos\theta(s,t) &= \frac{\sqrt{\left(1+\partial_s u(s,t)\right)^2+\left(\partial_s v(s,t)\right)^2}}{1+e},
\end{aligned} \tag{1}$$

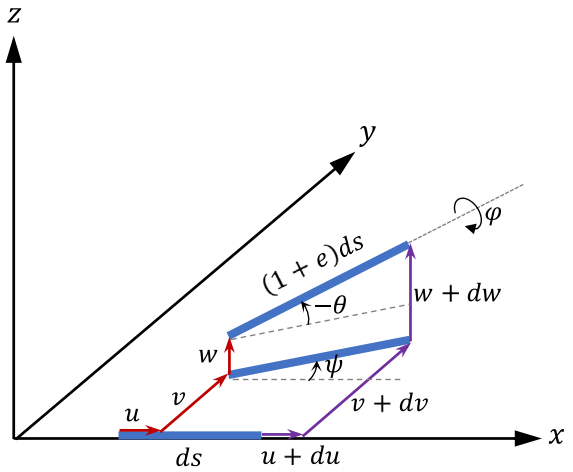

Fig. 1. Undeformed and deformed differential element of the beam showing displacements and Euler angles.

in which the operator ∂_s denotes $\partial/\partial s$.

It is important to note that even when the cantilever undergoes oscillations of extremely large amplitude, the strain remains small and hence the centreline can be safely assumed to remain inextensible, i.e. $e = 0$, which leads to $(1 + \partial_s u(s,t))^2 + (\partial_s v(s,t))^2 + (\partial_s w(s,t))^2 = 1$. As a result, the cantilever displacements u, v, and w, can be formulated in terms of the centreline rotation angles ψ and θ as

$$\begin{aligned} u(s,t) &= \int_0^s \Big(\cos\psi(\xi,t)\cos\theta(\xi,t) - 1\Big)\mathrm{d}\xi, \\ v(s,t) &= \int_0^s \sin\psi(\xi,t)\cos\theta(\xi,t)\mathrm{d}\xi, \\ w(s,t) &= -\int_0^s \sin\theta(\xi,t)\mathrm{d}\xi. \end{aligned} \tag{2}$$

Next, the strain and kinetic energies of the cantilever and the dissipative work of the viscous stresses are formulated. Denoting the deformed coordinate by $x^*y^*z^*$, the three curvature components about x^*, y^*, and z^* axes, represented by κ_1, κ_2, and κ_3, respectively, can be formulated in terms of the three Euler angles as [43]

$$\begin{aligned} \kappa_1(s,t) &= \partial_s\varphi(s,t) - \partial_s\psi(s,t)\sin\theta(s,t), \\ \kappa_2(s,t) &= \partial_s\psi(s,t)\cos\theta(s,t)\sin\varphi(s,t) + \partial_s\theta(s,t)\cos\varphi(s,t), \\ \kappa_3(s,t) &= \partial_s\psi(s,t)\cos\theta(s,t)\cos\varphi(s,t) - \partial_s\theta(s,t)\sin\varphi(s,t). \end{aligned} \tag{3}$$

A very important point to note here is that a nonzero φ is not necessarily an indication of the presence of a torque in the axial direction. In other words, even when there is no torque applied to the cantilever, the twist can be induced by bending deflections, and hence the reason that φ is considered in the model development. As a result, the following strains are defined

$$\varepsilon_{11}(s,t) = -y\kappa_3(s,t) + z\kappa_2(s,t), \quad \varepsilon_{12}(s,t) = -z\kappa_1(s,t), \quad \varepsilon_{13}(s,t) = y\kappa_1(s,t), \tag{4}$$

where ε_{12} and ε_{13} are engineering shear strains. The corresponding stress–strain relationships based on the Kelvin–Voigt model can be expressed as

$$\begin{aligned} \sigma_{11}(s,t) &= E\Big(\varepsilon_{11}(s,t) + \eta\partial_t\varepsilon_{11}(s,t)\Big), \\ \sigma_{12}(s,t) &= G\Big(\varepsilon_{12}(s,t) + \eta\partial_t\varepsilon_{12}(s,t)\Big), \\ \sigma_{13}(s,t) &= G\Big(\varepsilon_{13}(s,t) + \eta\partial_t\varepsilon_{13}(s,t)\Big), \end{aligned} \tag{5}$$

where η denotes the material viscosity.

The variation of the potential strain energy of the cantilever based on the elastic stress components is given by

$$\begin{aligned} \delta\mathcal{U}(t) &= \int_0^L \int_A \Big\{ E(-y\kappa_3(s,t) + z\kappa_2(s,t))(-y\delta\kappa_3(s,t) + z\delta\kappa_2(s,t)) \\ &\qquad + Gz^2\kappa_1(s,t)\delta\kappa_1(s,t) + Gy^2\kappa_1(s,t)\delta\kappa_1(s,t) \Big\}\mathrm{d}A\mathrm{d}s, \\ &= \int_0^L \Big\{ EI_z\kappa_3(s,t)\delta\kappa_3(s,t) + EI_y\kappa_2(s,t)\delta\kappa_2(s,t) + GI_x\kappa_1(s,t)\delta\kappa_1(s,t) \Big\}\mathrm{d}s, \end{aligned} \tag{6}$$

where δ represents the variational operator and

$$I_x = \int_A (y^2 + z^2)\mathrm{d}A, \quad I_y = \int_A z^2 \mathrm{d}A, \quad I_z = \int_A y^2 \mathrm{d}A. \tag{7}$$

It should be noted that the relationship $I_x = I_y + I_z$ holds only for homogeneous cantilevers with circular cross-sections. For cantilevers with non-circular cross-sections, the torsional rigidity GI_x reduces due to torsional warping of cross-sections [43].

Since the system is under harmonic base excitation in the y direction, the total displacement in the y direction is $v_t = v + y_0 \sin(\omega_y t)$. As such, the kinetic energy can be formulated as

$$\begin{aligned}\mathcal{K}_E = \frac{1}{2} m \int_0^L \Bigg\{ & \left[\int_0^s \Big(\partial_t \psi(\xi,t) \sin\psi(\xi,t) \cos\theta(\xi,t) + \partial_t \theta(\xi,t) \cos\psi(\xi,t) \sin\theta(\xi,t) \Big) \mathrm{d}\xi \right]^2 \\ & + \Bigg[y_0 \omega_y \cos(\omega_y t) + \int_0^s \Big(\partial_t \psi(\xi,t) \cos\psi(\xi,t) \cos\theta(\xi,t) \\ & - \partial_t \theta(\xi,t) \sin\psi(\xi,t) \sin\theta(\xi,t) \Big) \mathrm{d}\xi \Bigg]^2 \\ & + \left[\int_0^s \Big(\partial_t \theta(\xi,t) \cos\theta(\xi,t) \Big) \mathrm{d}\xi \right]^2 \Bigg\} \mathrm{d}s + \frac{1}{2} J_x \int_0^L \Big(\partial_t \varphi(s,t) \Big)^2 \mathrm{d}s, \end{aligned} \tag{8}$$

in which $J_x = \rho I_x$ where ρ is the mass density. It should be noted that the rotary inertias for ψ and θ are neglected, as they have negligible effect for slender cantilevers [43]. The reason for keeping the rotary inertia for φ is to ensure that all three equations of motion have inertia components, which makes the solution procedure more straightforward.

The virtual work of the viscous components of the stresses can be formulated as

$$\begin{aligned}\delta \mathcal{W}_v(t) = - \int_0^L \Big\{ & E\eta I_z \partial_t \kappa_3(s,t) \delta\kappa_3(s,t) + E\eta I_y \partial_t \kappa_2(s,t) \delta\kappa_2(s,t) \\ & + G\eta I_x \partial_t \kappa_1(s,t) \delta\kappa_1(s,t) \Big\} \mathrm{d}s. \end{aligned} \tag{9}$$

Substituting Eqs. (6), (8), and (9) into the extended Hamilton's principle

$$\int_{t_1}^{t_2} \Big(\delta\mathcal{K}_E(t) - \delta\mathcal{U}(t) + \delta\mathcal{W}_v(t) \Big) \mathrm{d}t = 0, \tag{10}$$

the equations of motion for ψ, θ, and φ can be obtained as

$$\begin{aligned} & m\cos\psi\cos\theta \int_s^L \left[-a_0 \sin(\omega_y t) + \int_0^{s^*} \partial_{tt} \Big(\sin\psi(\xi,t)\cos\theta(\xi,t) \Big) \mathrm{d}\xi \right] \mathrm{d}s^* \\ & - m\sin\psi\cos\theta \int_s^L \int_0^{s^*} \partial_{tt} \Big(\cos\psi(\xi,t)\cos\theta(\xi,t) - 1 \Big) \mathrm{d}\xi \mathrm{d}s^* \\ & - EI_z \partial_s \Big[\cos\theta\cos\varphi \Big(\kappa_3 + \eta\partial_t \kappa_3 \Big) \Big] \\ & - EI_y \partial_s \Big[\cos\theta\sin\varphi \Big(\kappa_2 + \eta\partial_t \kappa_2 \Big) \Big] + GI_x \partial_s \Big[\sin\theta \Big(\kappa_1 + \eta\partial_t \kappa_1 \Big) \Big] = 0, \end{aligned} \tag{11}$$

$$\begin{aligned} & m\cos\theta \int_s^L \int_0^{s^*} \partial_{tt} \Big(\sin\theta(\xi,t) \Big) \mathrm{d}\xi \mathrm{d}s^* \\ & - m\sin\psi\sin\theta \int_s^L \left[-a_0 \sin(\omega_y t) + \int_0^{s^*} \partial_{tt} \Big(\sin\psi(\xi,t)\cos\theta(\xi,t) \Big) \mathrm{d}\xi \right] \mathrm{d}s^* \\ & - m\cos\psi\sin\theta \int_s^L \int_0^{s^*} \partial_{tt} \Big(\cos\psi(\xi,t)\cos\theta(\xi,t) - 1 \Big) \mathrm{d}\xi \mathrm{d}s^* \\ & - GI_x (\partial_s \psi) \cos\theta \Big(\kappa_1 + \eta\partial_t \kappa_1 \Big) \\ & - EI_z \Big[(\partial_s \psi) \sin\theta\cos\varphi \Big(\kappa_3 + \eta\partial_t \kappa_3 \Big) \Big] - EI_y \Big[(\partial_s \psi) \sin\theta\sin\varphi \Big(\kappa_2 + \eta\partial_t \kappa_2 \Big) \Big] \\ & + EI_z \partial_s \Big[\sin\varphi \Big(\kappa_3 + \eta\partial_t \kappa_3 \Big) \Big] - EI_y \partial_s \Big[\cos\varphi \Big(\kappa_2 + \eta\partial_t \kappa_2 \Big) \Big] = 0, \end{aligned} \tag{12}$$

$$\begin{aligned} & J_x \partial_{tt} \varphi - GI_x \partial_s \big(\kappa_1 + \eta\partial_t \kappa_1 \big) - EI_z \Big[\big(\partial_s \psi \cos\theta \sin\varphi + \partial_s \theta \cos\varphi \big) \big(\kappa_3 + \eta\partial_t \kappa_3 \big) \Big] \\ & \quad + EI_y \Big[\big(\partial_s \psi \cos\theta \cos\varphi - \partial_s \theta \sin\varphi \big) \big(\kappa_2 + \eta\partial_t \kappa_2 \big) \Big] = 0. \end{aligned} \tag{13}$$

in which a_0 is the base acceleration in the y direction which is related to the base excitation amplitude and frequency via $a_0 = y_0 \omega_y^2$.

It is more convenient to analyse the equations of motion in dimensionless form. Hence, the following dimensionless parameters are defined

$$\begin{aligned} &\tilde{s} = \frac{s}{L}, \quad \beta_1 = \frac{GI_x}{EI_z}, \quad \beta_2 = \frac{I_y}{I_z}, \quad \chi = \frac{J_x}{mL^2}, \\ &\tau = \frac{t}{T}, \quad \Omega_y = \omega_y T, \quad \eta_d = \frac{\eta}{T}, \quad a_y = \frac{a_0 T^2}{L}, \end{aligned} \tag{14}$$

where $T = \left(\frac{m}{EI}\right)^{\frac{1}{2}} L^2$. Substituting these quantities into Eqs. (11)–(13), the dimensionless geometrically-exact equations of motion of the cantilever can be obtained as

$$\begin{aligned} &\cos\psi\cos\theta \int_{\bar{s}}^{1} \left[-a_y \sin(\Omega_y \tau) + \int_0^{s^*} \partial_{\tau\tau}\Big(\sin\psi(\xi,t)\cos\theta(\xi,t)\Big)\mathrm{d}\xi\right]\mathrm{d}s^* \\ &- \sin\psi\cos\theta \int_{\bar{s}}^{1}\int_0^{s^*} \partial_{\tau\tau}\Big(\cos\psi(\xi,t)\cos\theta(\xi,t) - 1\Big)\mathrm{d}\xi\mathrm{d}s^* \\ &- \partial_{\bar{s}}\left\{\cos\theta\cos\varphi\left[\partial_{\bar{s}}\psi\cos\theta\cos\varphi - \partial_{\bar{s}}\theta\sin\varphi + \eta_d\partial_\tau\Big(\partial_{\bar{s}}\psi\cos\theta\cos\varphi - \partial_{\bar{s}}\theta\sin\varphi\Big)\right]\right\} \\ &- \beta_2\partial_{\bar{s}}\left\{\cos\theta\sin\varphi\left[\partial_{\bar{s}}\psi\cos\theta\sin\varphi + \partial_{\bar{s}}\theta\cos\varphi + \eta_d\partial_\tau\Big(\partial_{\bar{s}}\psi\cos\theta\sin\varphi + \partial_{\bar{s}}\theta\cos\varphi\Big)\right]\right\} \\ &+ \beta_1\partial_{\bar{s}}\left\{\sin\theta\left[\partial_{\bar{s}}\varphi - \partial_{\bar{s}}\psi\sin\theta + \eta_d\partial_\tau\Big(\partial_{\bar{s}}\varphi - \partial_{\bar{s}}\psi\sin\theta\Big)\right]\right\} = 0, \end{aligned} \tag{15}$$

$$\begin{aligned} &\cos\theta\int_{\bar{s}}^{1}\int_0^{s^*} \partial_{\tau\tau}\Big(\sin\theta(\xi,\tau)\Big)\mathrm{d}\xi\mathrm{d}s^* \\ &- \cos\psi\sin\theta\int_{\bar{s}}^{1}\int_0^{s^*} \partial_{\tau\tau}\Big(\cos\psi(\xi,t)\cos\theta(\xi,t) - 1\Big)\mathrm{d}\xi\mathrm{d}s^* \\ &- \sin\psi\sin\theta\int_{\bar{s}}^{1}\left[-a_y\sin(\Omega_y\tau) + \int_0^{s^*}\partial_{\tau\tau}\Big(\sin\psi(\xi,t)\cos\theta(\xi,t)\Big)\mathrm{d}\xi\right]\mathrm{d}s^* \\ &- \beta_1(\partial_{\bar{s}}\psi)\cos\theta\left[\partial_{\bar{s}}\varphi - \partial_{\bar{s}}\psi\sin\theta + \eta_d\partial_\tau\Big(\partial_{\bar{s}}\varphi - \partial_{\bar{s}}\psi\sin\theta\Big)\right] \\ &- (\partial_{\bar{s}}\psi)\sin\theta\cos\varphi\left[\partial_{\bar{s}}\psi\cos\theta\cos\varphi - \partial_{\bar{s}}\theta\sin\varphi + \eta_d\partial_\tau\Big(\partial_{\bar{s}}\psi\cos\theta\cos\varphi - \partial_{\bar{s}}\theta\sin\varphi\Big)\right] \\ &- \beta_2(\partial_{\bar{s}}\psi)\sin\theta\sin\varphi\left[\partial_{\bar{s}}\psi\cos\theta\sin\varphi + \partial_{\bar{s}}\theta\cos\varphi + \eta_d\partial_\tau\Big(\partial_{\bar{s}}\psi\cos\theta\sin\varphi + \partial_{\bar{s}}\theta\cos\varphi\Big)\right] \\ &+ \partial_{\bar{s}}\left\{\sin\varphi\left[\partial_{\bar{s}}\psi\cos\theta\cos\varphi - \partial_{\bar{s}}\theta\sin\varphi + \eta_d\partial_\tau\Big(\partial_{\bar{s}}\psi\cos\theta\cos\varphi - \partial_{\bar{s}}\theta\sin\varphi\Big)\right]\right\} \\ &- \beta_2\partial_{\bar{s}}\left\{\cos\varphi\left[\partial_{\bar{s}}\psi\cos\theta\sin\varphi + \partial_{\bar{s}}\theta\cos\varphi + \eta_d\partial_\tau\Big(\partial_{\bar{s}}\psi\cos\theta\sin\varphi + \partial_{\bar{s}}\theta\cos\varphi\Big)\right]\right\} = 0, \end{aligned} \tag{16}$$

$$\begin{aligned} &\chi\partial_{\tau\tau}\varphi - \beta_1\partial_{\bar{s}}\left[\partial_{\bar{s}}\varphi - \partial_{\bar{s}}\psi\sin\theta + \eta_d\partial_\tau\Big(\partial_{\bar{s}}\varphi - \partial_{\bar{s}}\psi\sin\theta\Big)\right] \\ &- \Big(\partial_{\bar{s}}\psi\cos\theta\sin\varphi + \partial_{\bar{s}}\theta\cos\varphi\Big)\Big[\partial_{\bar{s}}\psi\cos\theta\cos\varphi - \partial_{\bar{s}}\theta\sin\varphi \\ &\qquad + \eta_d\partial_\tau\Big(\partial_{\bar{s}}\psi\cos\theta\cos\varphi - \partial_{\bar{s}}\theta\sin\varphi\Big)\Big] \\ &+ \beta_2\Big(\partial_{\bar{s}}\psi\cos\theta\cos\varphi - \partial_{\bar{s}}\theta\sin\varphi\Big)\Big[\partial_{\bar{s}}\psi\cos\theta\sin\varphi + \partial_{\bar{s}}\theta\cos\varphi \\ &\qquad + \eta_d\partial_\tau\Big(\partial_{\bar{s}}\psi\cos\theta\sin\varphi + \partial_{\bar{s}}\theta\cos\varphi\Big)\Big] = 0. \end{aligned} \tag{17}$$

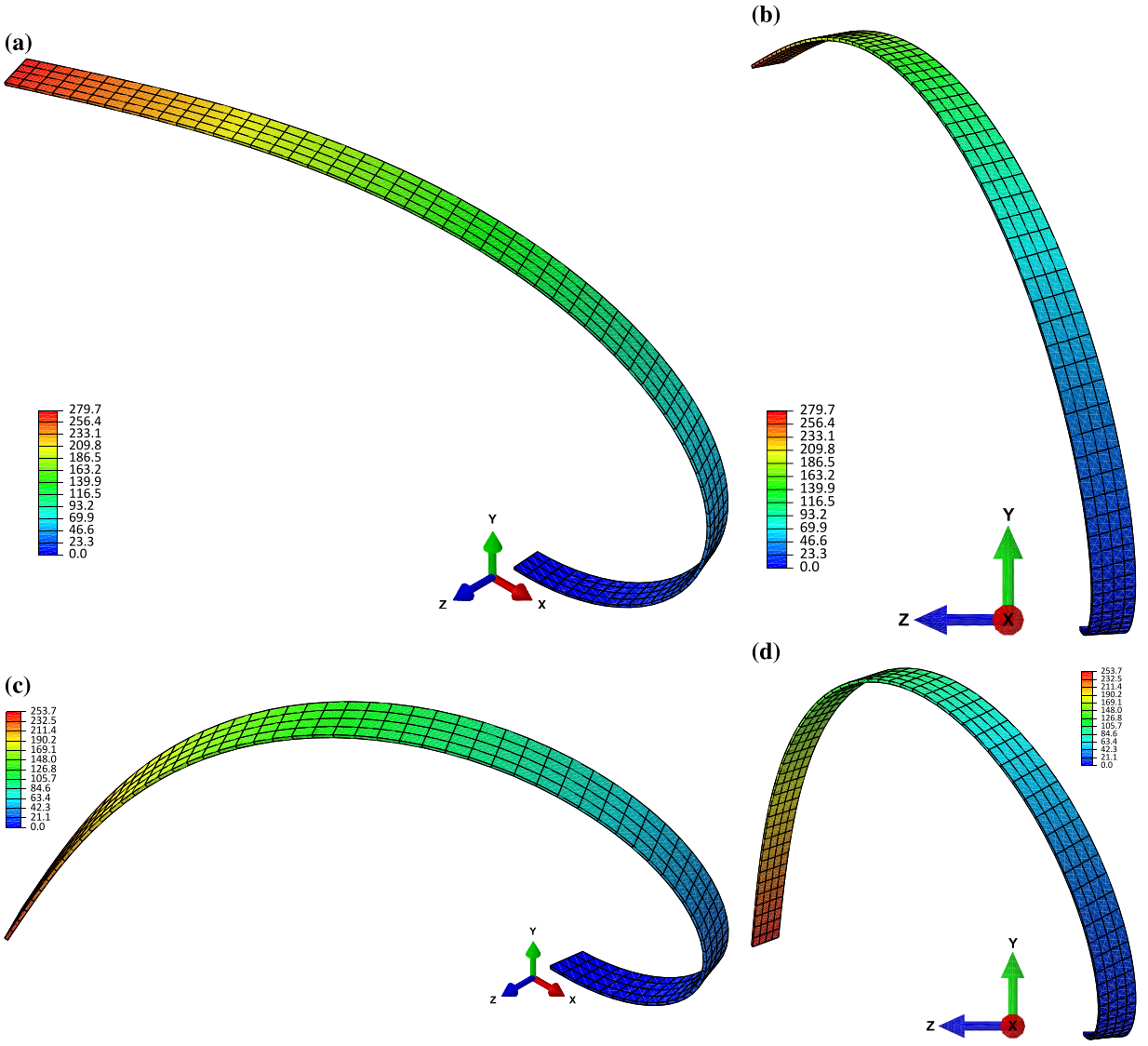

Fig. 2. Contour plots of the total displacement magnitude (in mm) of the cantilever. (a, b) 3D and 2D (yz plane) views at $f_d = 6$; (c, d) 3D and 2D (yz plane) views at $f_d = 9$.

3. Discretisation and solution technique

The first step toward solving the nonlinear integro-partial differential equations of the geometrically exact model, i.e. Eqs. (15)–(17), is the spatial discretisation via the Galerkin technique. To this end, the Euler angles ψ, θ, and φ are defined as

$$\begin{aligned}\psi(\tilde{s},\tau) &= \sum_{n=1}^{N_1} \Xi_n(\tilde{s}) q_n(\tau),\\ \theta(\tilde{s},\tau) &= \sum_{n=1}^{N_2} \Xi_n(\tilde{s}) p_n(\tau),\\ \varphi(\tilde{s},\tau) &= \sum_{n=1}^{N_3} \boldsymbol{\Phi}_n(\tilde{s}) r_n(\tau),\end{aligned} \tag{18}$$

in which $q_n(\tau)$, $p_n(\tau)$, and $r_n(\tau)$ denote the unknown time-dependent generalised coordinates of centreline rotations ψ, θ, and φ, respectively. $\Xi_n(\tilde{s})$ is defined as $\partial_{\tilde{s}} Y_n(\tilde{s})/\alpha_n$, where $Y_n(\tilde{s})$ is the nth linear eigenfunction for the transverse motion of a cantilever and α_n is the nth root of the transcendental equation $1 + \cosh(\alpha)\cos(\alpha) = 0$. Furthermore, $\boldsymbol{\Phi}_n(\tilde{s}) = \sin[(n - 1/2)\pi\tilde{s}]$.

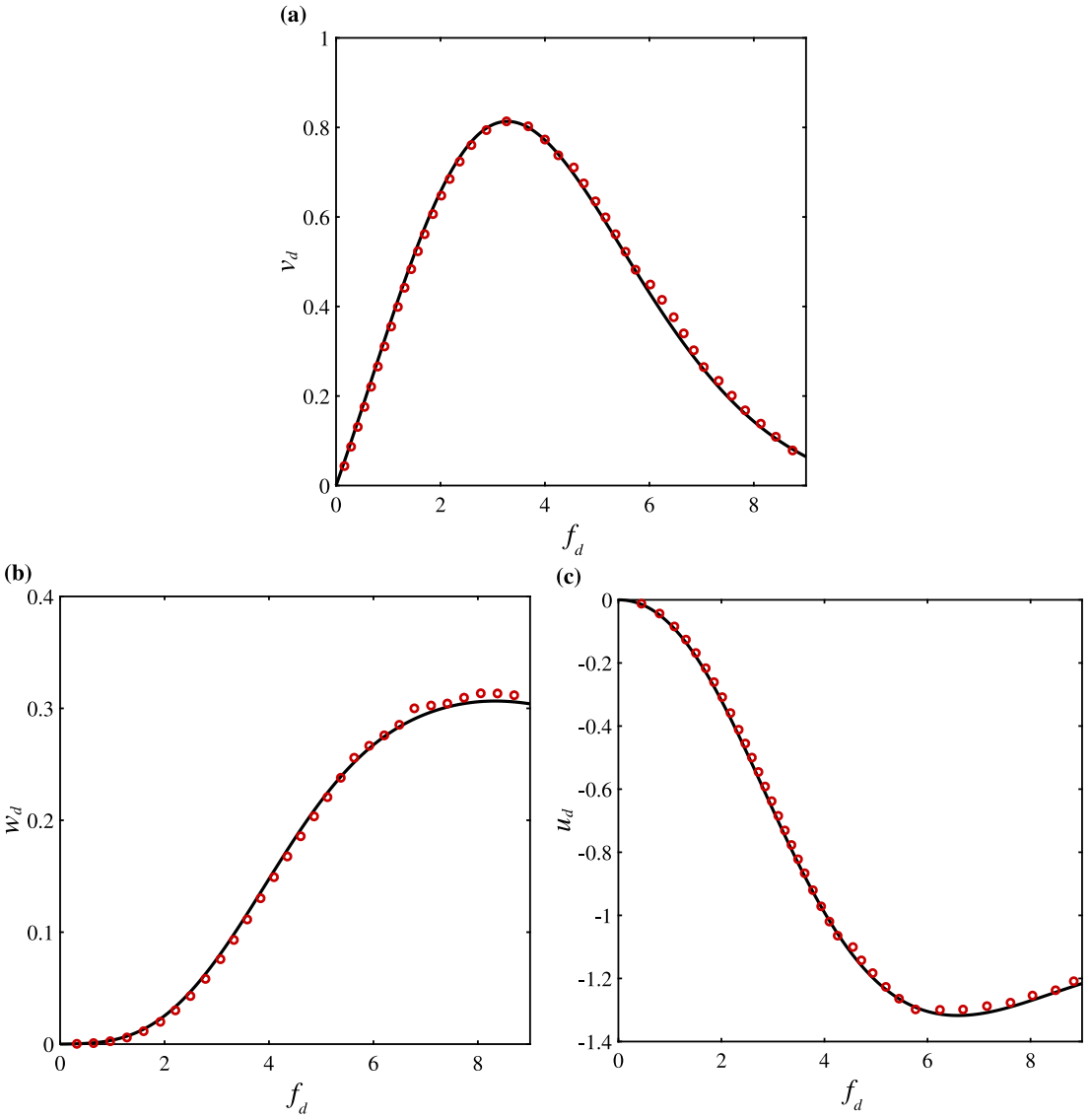

Fig. 3. Nonlinear static deflection of the cantilever tip under the follower tip loads of $\tilde{f}_1 = \tilde{f}_2 = f_d$ and $\tilde{f}_3 = f_d/4$. (a, b) transverse tip displacements in the y and z directions, respectively, and (c) longitudinal tip displacement. Solid line: the proposed geometrically exact model; symbols: the 3D nonlinear FE model.

In this study, an 18-degree-of-freedom (dof) model is constructed by setting $N_1 = N_2 = N_3 = 6$, i.e. by retaining the first 6 modes for each rotation angle. This number of degrees of freedom ensures converged results as further discussed in Section 6. The key challenge in discretising the geometrically exact equations of motion is that unlike the case of truncated nonlinear models, for the exact model the integrations over the spatial domain cannot be carried out in closed-form and hence need to be performed numerically while retaining sufficient number of terms to ensure convergence. This yields a set of very large discretised equations, but ensures reliable results even at extremely large oscillation amplitudes.

The discretised model consisting of a set of 18 second-order nonlinear ordinary differential equations (ODEs) is first transformed into a system of 36 first-order ODEs, and the resultant set is solved via a pseudo-arclength continuation technique. It should be highlighted here that the unique advantage of deriving the equations of motion for centreline rotations, rather than centreline displacements, is that it allows examining oscillations of extremely large amplitudes, even for cases when the tip of the cantilever is bent backwards. Such behaviours cannot be captured or analysed using a nonlinear truncated model irrespective of the order of truncation, due to the inherent limitation of such models to angles in the range of $[-\pi/2\ \pi/2]$. After solving the discretised set of equations for centreline rotations and obtaining the generalised coordinates, the centreline displacements are obtained via Eq. (2).

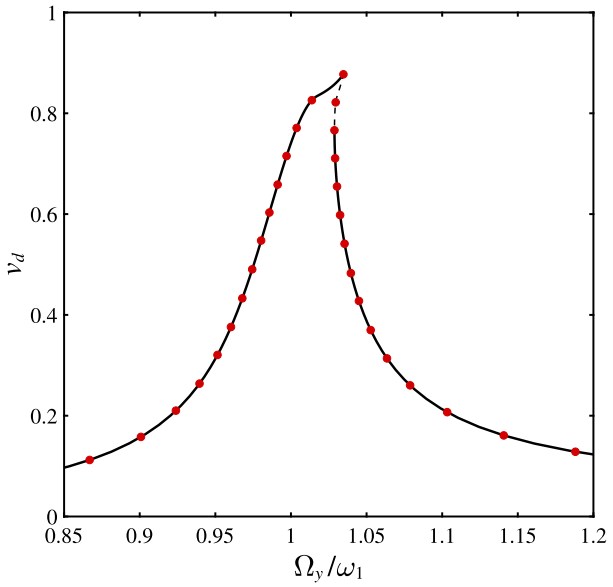

Fig. 4. Comparison between the 2D resonance response of a cantilever obtained using the exact model proposed in the present study to that reported in Ref. [29] using an exact 2D model. Solid line: present study; symbols: Ref. [29].

4. Verification

In this section, the accuracy of the proposed geometrically exact model is verified for both static and dynamic cases. More specifically, first a comparison is performed between the proposed 3D geometrically exact model and a 3D nonlinear finite element model in predicting the extreme 3D static deflection of a cantilever. The proposed model is then verified for a dynamic case via comparison to the 2D exact model in Ref. [29], to verify the accuracy of the proposed model for the case of 2D motion.

Starting with the verification for the static case, a cantilevered beam is considered which is subject to three follower tip loads of f_1, f_2, and f_3 in the directions x^*, y^*, and z^*, respectively, with $x^*y^*z^*$ being the local deformed coordinate. Such follower loads are considered to ensure the beam undergoes a three-dimensional deformation. Calculating the components of the follower loads in the undeformed coordinate xyz, their virtual work can be formulated as

$$\begin{aligned}\delta\mathcal{W}_f(t) = \int_0^L \Big\{ &\Big[f_1\cos\theta\cos\psi + f_2\big(-\cos\varphi\sin\psi + \sin\varphi\sin\theta\cos\psi\big) \\ &+ f_3\big(\sin\varphi\sin\psi + \cos\varphi\sin\theta\cos\psi\big)\Big]\,\delta_D(s-L)\delta u \\ &+ \Big[f_1\cos\theta\sin\psi + f_2\big(\cos\varphi\cos\psi + \sin\varphi\sin\theta\sin\psi\big) \\ &+ f_3\big(-\sin\varphi\cos\psi + \cos\varphi\sin\theta\sin\psi\big)\Big]\,\delta_D(s-L)\delta v \\ &+ \Big[-f_1\sin\theta + f_2\sin\varphi\cos\theta + f_3\cos\varphi\cos\theta\Big]\delta_D(s-L)\delta w \Big\}\,\mathrm{d}s,\end{aligned} \tag{19}$$

where δ_D indicates the Dirac delta function. Substituting for δu, δv, and δw using Eq. (2), and inserting Eq. (19) into extended Hamilton's principle leads to additional terms for Eqs. (11) and (12). Transforming these terms into dimensionless form, the following terms need to be added to the Eqs. (15) and (16), respectively

$$\begin{aligned}\delta\psi:\quad &\cos\theta\sin\psi\int_{\bar{s}}^1 f_u\delta_D(s^*-1)\mathrm{d}s^* - \cos\theta\cos\psi\int_{\bar{s}}^1 f_v\delta_D(s^*-1)\mathrm{d}s^*, \\ \delta\theta:\quad &\sin\theta\cos\psi\int_{\bar{s}}^1 f_u\delta_D(s^*-1)\mathrm{d}s^* + \sin\theta\sin\psi\int_{\bar{s}}^1 f_v\delta_D(s^*-1)\mathrm{d}s^* \\ &+\cos\theta\int_{\bar{s}}^1 f_w\delta_D(s^*-1)\mathrm{d}s^*,\end{aligned} \tag{20}$$

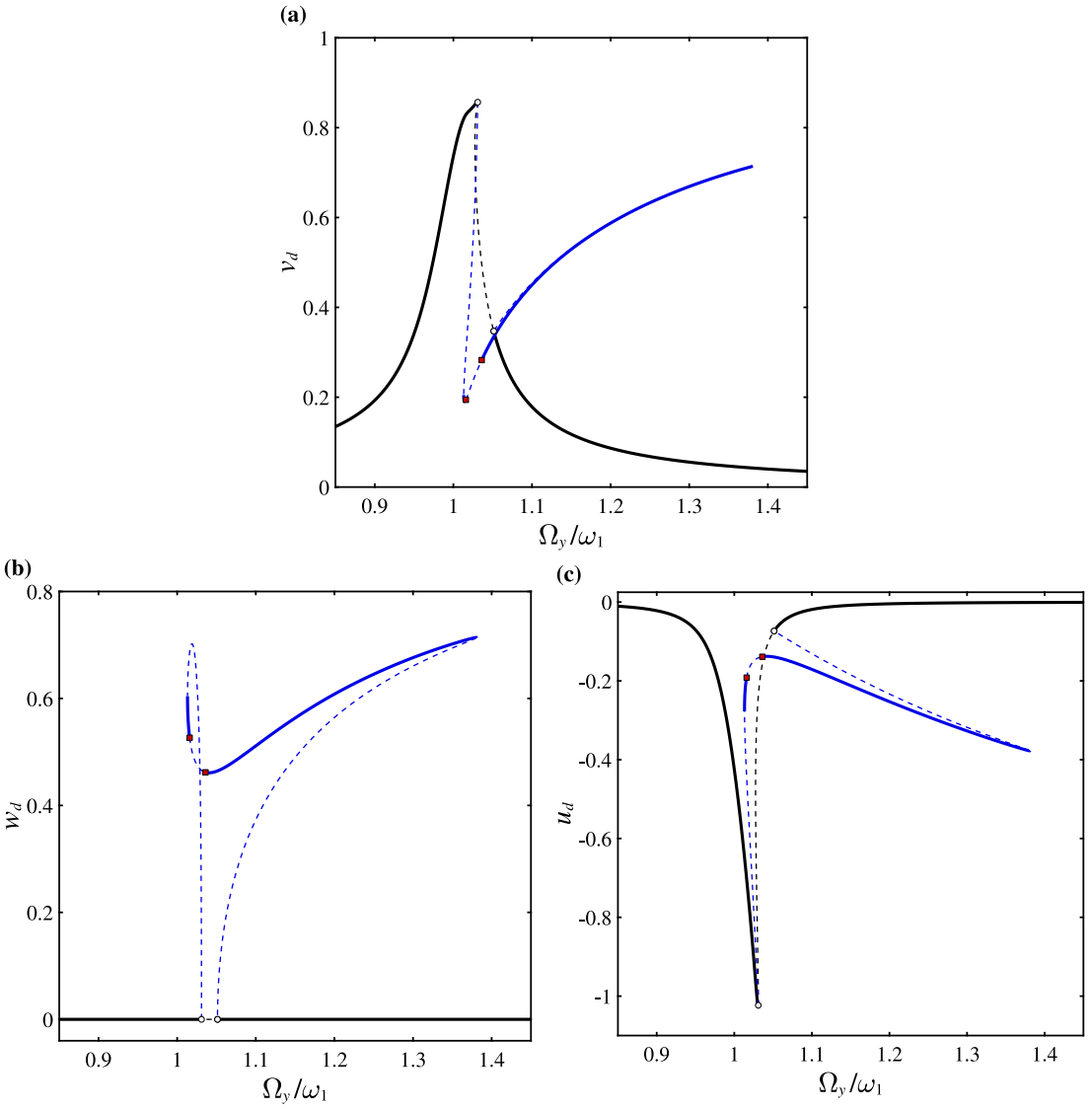

Fig. 5. Frequency–amplitude diagrams of the cantilevered beam showing (a, b) the maximum tip transverse motions in y and z directions, respectively, and (c) the minimum tip longitudinal motion. [▬] Stable periodic solution, [- - -] unstable periodic solution. Squares and circles denote torus bifurcations and branch points, respectively. $a_y = 0.30$.

in which

$$
\begin{aligned}
f_u &= \tilde{f}_1 \cos\theta \cos\psi + \tilde{f}_2\big(-\cos\varphi \sin\psi + \sin\varphi \sin\theta \cos\psi\big) + \tilde{f}_3\big(\sin\varphi \sin\psi + \cos\varphi \sin\theta \cos\psi\big),\\
f_v &= \tilde{f}_1 \cos\theta \sin\psi + \tilde{f}_2\big(\cos\varphi \cos\psi + \sin\varphi \sin\theta \sin\psi\big) + \tilde{f}_3\big(-\sin\varphi \cos\psi + \cos\varphi \sin\theta \sin\psi\big),\\
f_w &= -\tilde{f}_1 \sin\theta + \tilde{f}_2 \sin\varphi \cos\theta + \tilde{f}_3 \cos\varphi \cos\theta,
\end{aligned}
\tag{21}
$$

where $\tilde{f}_i = f_i L^2/EI_z$ $(i = 1, 2, 3)$. This exact model is then discretised following the procedure outlined in Section 3.

The 3D nonlinear static finite element (FE) analysis [45,46] is conducted via Abaqus/CAE, using the 8-node quadrilateral continuum shell element with reduced integration. A cantilever with the following dimensions is considered: $L = 200$ mm, $h = 0.5$ mm, and $b = 6$ mm. The nonlinear static deformation of the cantilever is obtained via the FE model as well as the geometrically exact model. The results are reported in dimensionless form, i.e. dimensionless force f_d which is related to $\tilde{f}_1$, $\tilde{f}_2$, and $\tilde{f}_3$ via $\tilde{f}_1 = \tilde{f}_2 = f_d$ and $\tilde{f}_3 = f_d/4$, and dimensionless displacements $u_d = u/L$, $v_d = v/L$, and $w_d = w/L$.

Another note that should be made here is that, since the cantilever cross-section is non-circular for the static verification case, I_x is not equal to $I_y + I_z$. Hence, the following formulation for a rectangular cross-section of width b and thickness h is used to

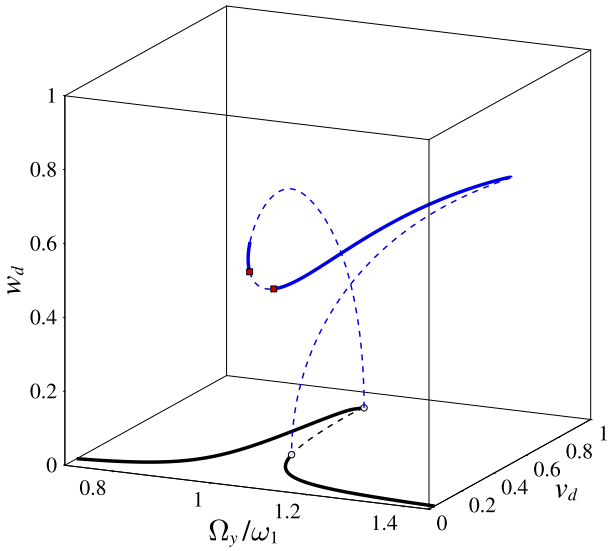

Fig. 6. Three-dimensional frequency–amplitude diagram of the system of Fig. 5 showing regions of 2D and 3D motion. [▬] Stable periodic solution, [- - -] unstable periodic solution. Squares and circles denote torus bifurcations and branch points, respectively.

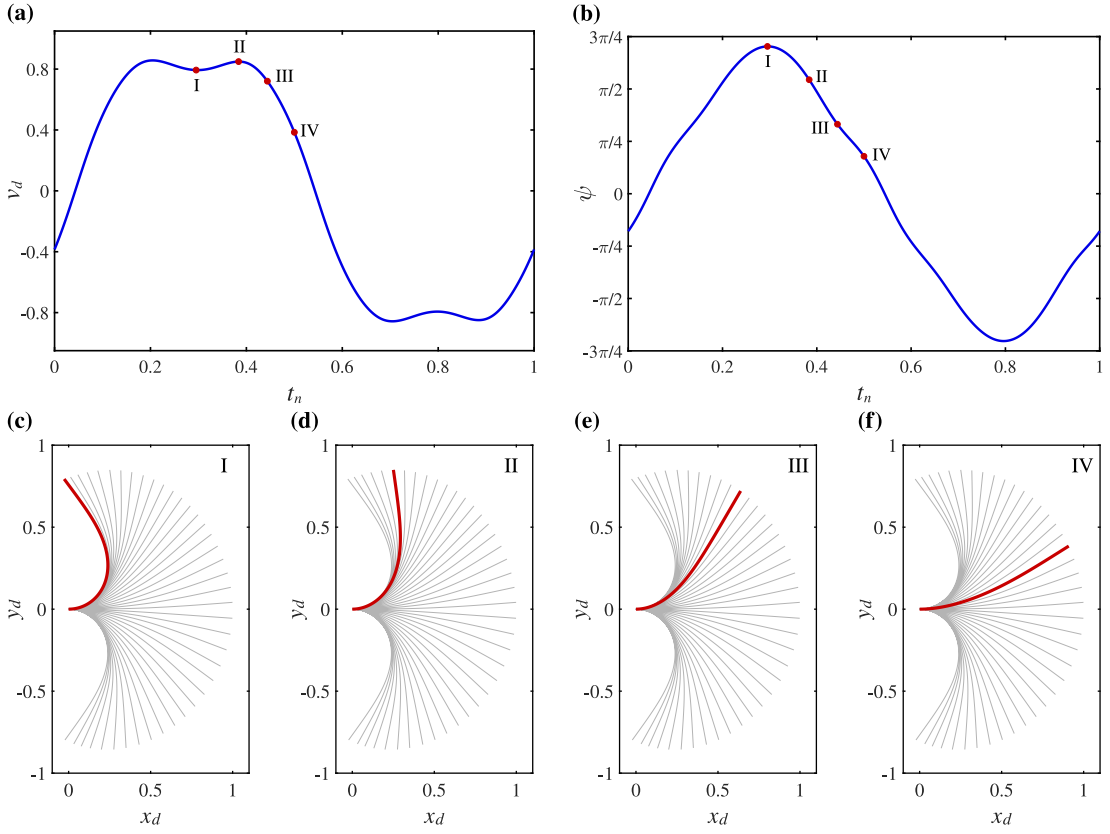

Fig. 7. Detailed dynamical response of the system of Fig. 5 at $\Omega_y/\omega_1 = 1.0308$ (peak amplitude at 2D motion region). (a, b) Time histories of v_d and ψ in one period of oscillation, respectively (t_n: time normalised relative to oscillation period). (c–f) Snapshots of the oscillation of the cantilever at points I–IV, respectively.

calculate I_x [47]

$$I_x = \frac{1}{3}bh^3\left(1 - \frac{192h}{\pi^5 b}\sum_{n=1}^{\infty}\frac{1}{(2n-1)^5}\tanh\frac{(2n-1)\pi b}{2h}\right), \tag{22}$$

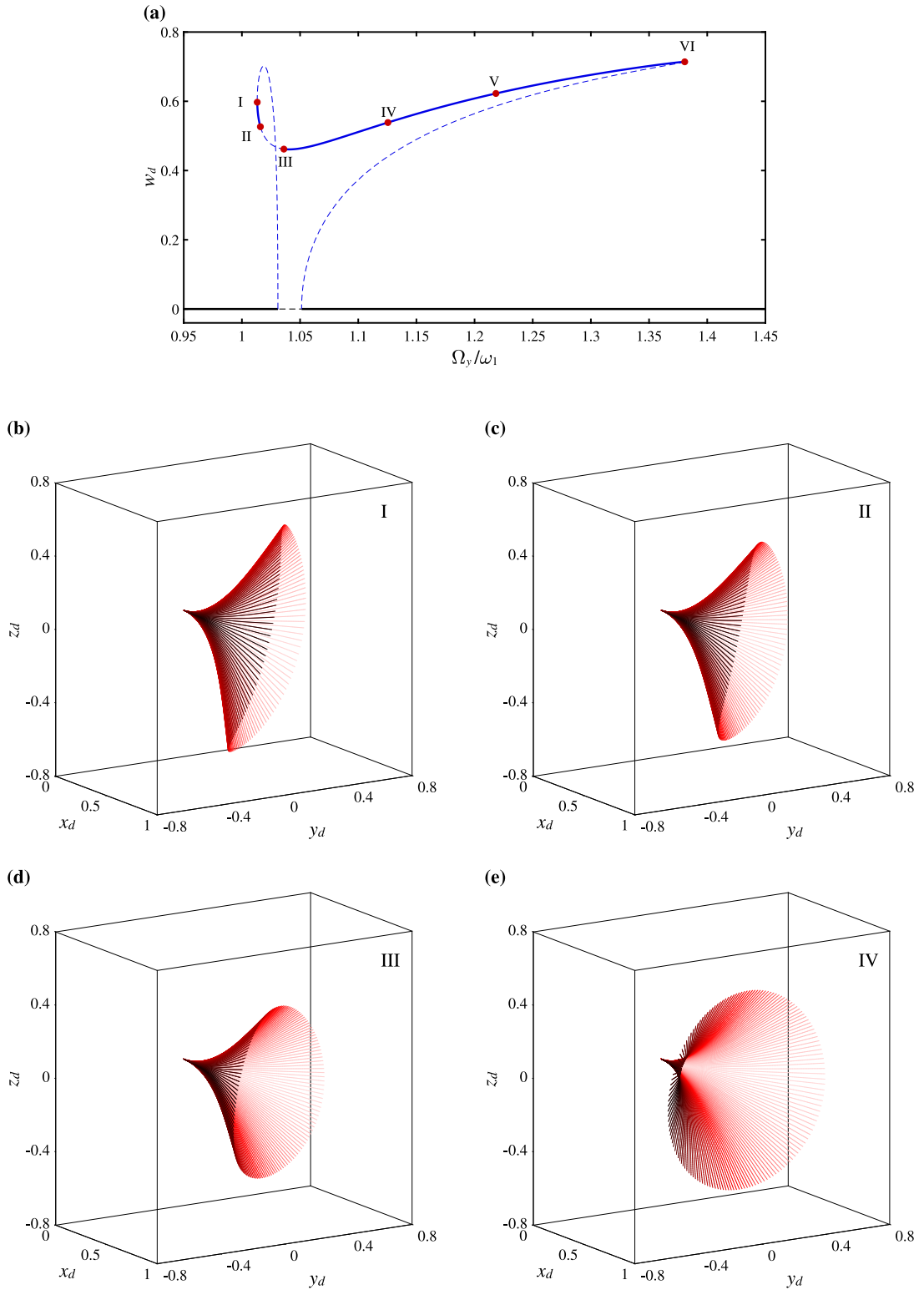

Fig. 8. Dynamical response of the system of Fig. 5 at various oscillation frequencies (3D region). (a) Out-of-plane transverse motion frequency–amplitude diagram. (b–g) 3D oscillations of the cantilever at points I–VI, respectively.

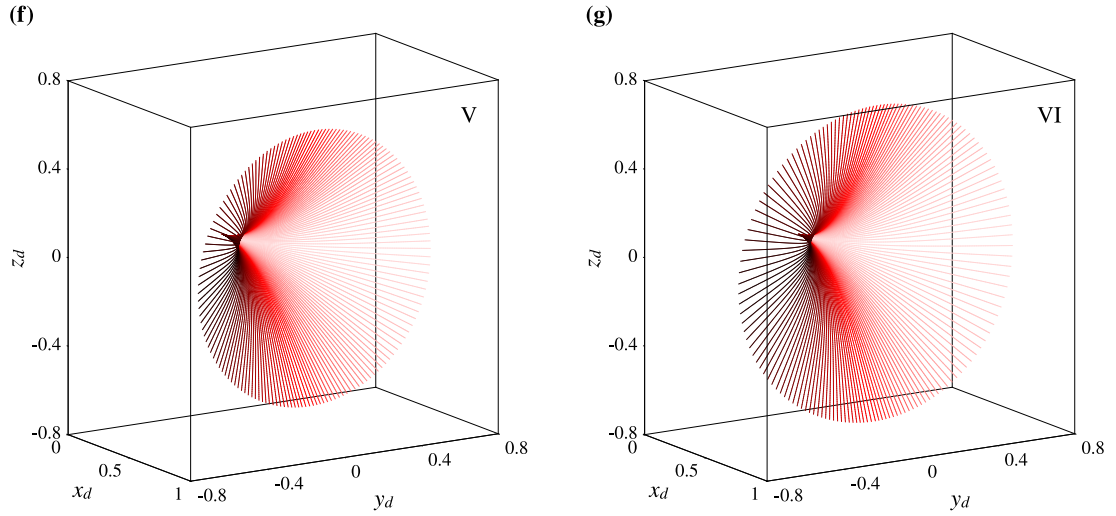

Fig. 8. (*continued*).

while retaining sufficient terms to ensure a converged value for I_x.

The FE results at $f_d = 6$ and $f_d = 9$ are shown in Fig. 2, highlighting the extreme 3D deformation of the cantilever. To compare the FE results to those obtained by the geometrically exact model, the displacements of the tip of the cantilever in the x, y, and z directions are calculated by the two models and plotted in Fig. 3. It is seen that the static deflections predicted by the geometrically exact model are very close to those obtained by the nonlinear 3D FE model even at extremely large 3D deflections, which verifies the accuracy of the proposed exact model.

Next, a comparison is conducted between the proposed 3D exact model and the 2D exact model in Ref. [29], and the result is shown in Fig. 4. This comparison is conducted to verify the accuracy of the proposed model for the case of 2D motions of extremely large amplitude. The reason for comparing to a 2D model is that, to the authors' best knowledge, there is currently no 3D exact model of a cantilever available in the literature, and the present study is the first to propose one. The system parameters are set to those used in Ref. [29]. Furthermore, β_2 is set to 10 in the 3D model to ensure that the cantilever motion remains in the 2D regime. As seen in Fig. 4, the proposed model predicts the same primary resonance response as the 2D exact model in Ref. [29], which verifies the accuracy of the proposed model in capturing extremely large oscillations.

5. Results and discussion

In this section, extensive numerical results are presented and the three-dimensional exact nonlinear dynamics of the cantilever is examined and discussed in detail. For all the cases examined in this section, it is assumed that the cantilever has a circular cross-section, and unless otherwise specified, the following values are used: $\beta_1 = 0.77$, $\beta_2 = 1$, $\chi = 5.0\text{e}{-7}$, and $\eta_d = 0.004$. Similar to the previous section, the results are presented in terms dimensionless displacements, namely $u_d = u/L$, $v_d = v/L$, and $w_d = w/L$. Additionally, ω_1 represents the first dimensionless natural frequency of the cantilever which is related to its dimensional counterpart $\bar{\omega}_1$ via $\omega_1 = \bar{\omega}_1 T$. Furthermore, x_d, y_d, and z_d represent the dimensionless coordinates (with respect to L) associated with the undeformed geometry.

Fig. 5 shows the nonlinear frequency–amplitude diagrams of the cantilever in the primary resonance region for the case when $a_y = 0.30$. It is seen that even though the cantilever is being excited only in the y direction (i.e. in-plane transverse direction), due to presence of one-to-one internal resonances between the in-plane and out-of-plane transverse modes, bifurcation points occur which give rise to out-of-plane transverse motion. It should be noted that these bifurcation points (here referred to as branch points, and shown by circles on the diagrams) only appear at sufficiently large base-acceleration amplitudes. In other words, for relatively small values of a_y, the motion remains planar (i.e. two-dimensional). As seen, the cantilever displays weakly hardening nonlinear behaviour in regions of planar 2D motion; however, the hardening nonlinearity is much stronger when the beam is undergoing three-dimensional motion. As seen, the cantilever undergoes oscillations of extremely large amplitude. In particular, in the 2D region, the cantilever reaches a maximum transverse amplitude of 0.86, after which a saddle–node bifurcation occurs rendering the system unstable and causing a jump to lower-energy branch. In the 3D resonance region, the in-plane and out-of-plane transverse motions reach a similar maximum amplitude of 0.71 at $\Omega_y/\omega_1 = 1.38$, which corresponds to the occurrence of another saddle–node bifurcation.

In order to better illustrate the 2D and 3D motion regions, the 3D frequency–amplitude plot of the cantilever is constructed in Fig. 6. This figure shows the maximum in-plane and out-of-plane transverse amplitudes as a function of the base-excitation frequency ratio. The figure clearly shows the branch points that give rise to 3D motion as well as regions of 2D and 3D motion.

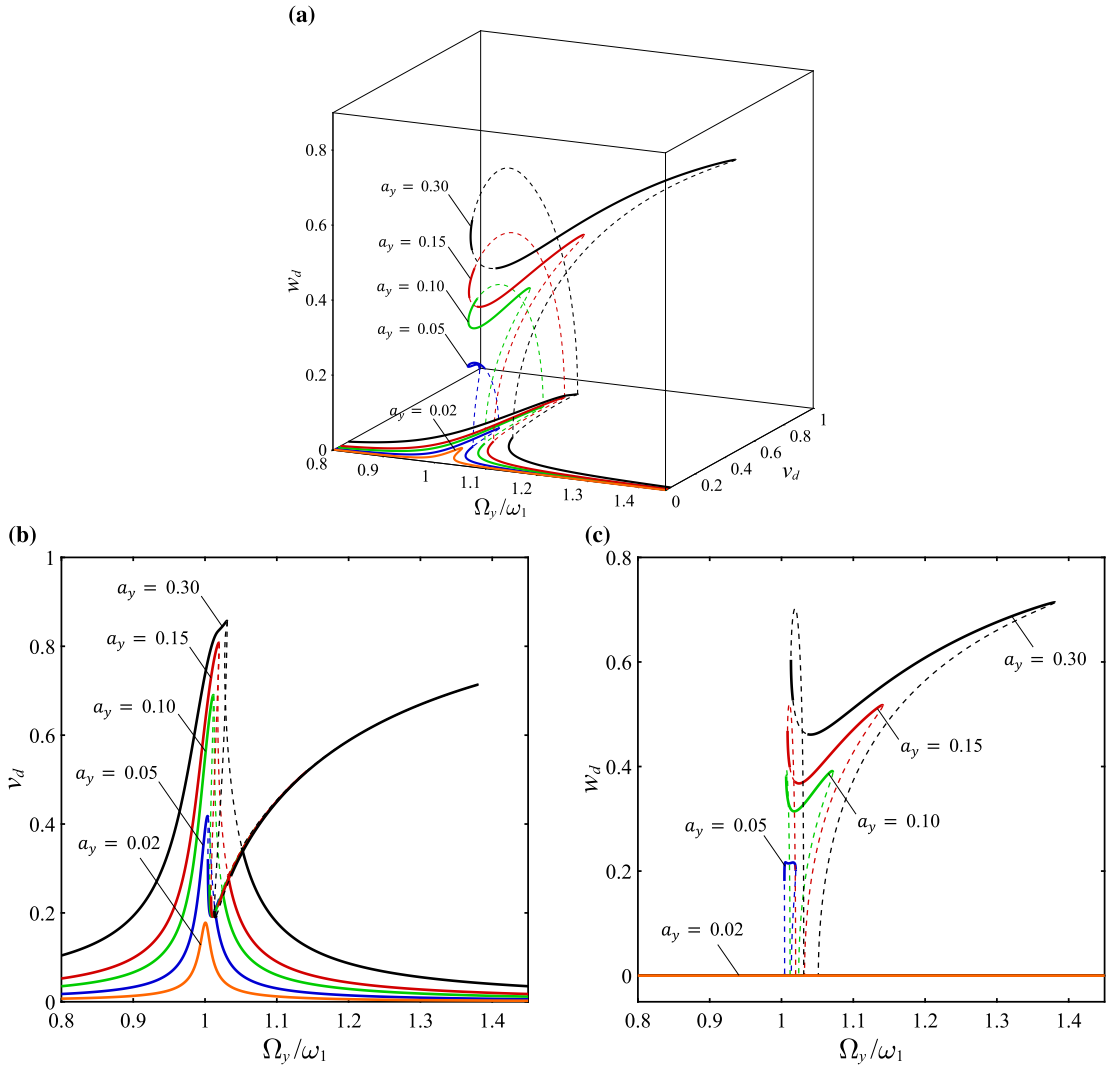

Fig. 9. Frequency–amplitude diagrams of the cantilevered beam for several base-acceleration amplitudes. (a) Three-dimensional diagram; (b, c) transverse motions in the y and z directions, respectively. [▬] Stable periodic solution, [- - -] unstable periodic solution.

One of the key features of the proposed 3D geometrically exact cantilever model is its capability of capturing extremely large oscillations. To better illustrate this, Figs. 7 and 8 are constructed showing the extreme vibrations of the cantilever in regions of 2D and 3D motion. More specifically, Fig. 7(a, b) show the time histories of the in-plane transverse motion v_d and centreline rotation ψ for the tip of the cantilever in one period of oscillation at peak amplitude of the 2D motion region at $\Omega_y/\omega_1 = 1.0308$. Snapshots of the state of the cantilever at points I–IV are shown in sub-figures (c)–(f), respectively, by a red line, while showing the oscillation range in one period by light grey lines. It is seen that slope of the tip, i.e. ψ, reaches its maximum at I; however, that does not corresponds to maximum in-plane tip transverse oscillation amplitude. This is due to the fact the cantilever oscillation is so large that the tip of the cantilever bends backwards. As a result, the in-plane tip transverse amplitude increases initially until reaching a maximum (at II) and then decreases due to tip bending backwards.

The detailed 3D oscillations of the cantilever in one period at various frequencies are shown in Fig. 8. To better show the changes in the in-plane and out-of-plane transverse amplitudes of the 3D motion as the frequency of the base-excitation is increased, Fig. 5(a) is shown here again in sub-figure (a), on which six points are highlighted. The 3D oscillations at these points are then plotted in subsequent sub-figures. As can be seen, at smaller frequency ratios (i.e. cases I–III), the out-of-plane transverse motion amplitude is larger than the in-plane one, hence the tip motion path creating an oval shape. At larger frequency ratios, on the other hand, the difference between the in-plane and out-of-plane transverse motion amplitudes decreases, hence the tip creates a circular path.

The effect of the base-acceleration amplitude on the 3D primary resonance response of the cantilever is illustrated in Fig. 9. The figure shows that, at relatively small base-acceleration amplitudes, i.e. $a_y = 0.02$, no branch points occur and hence the motion stays 2D in the primary resonance region. In other words, a base-excitation in the y direction will lead to oscillation only in the

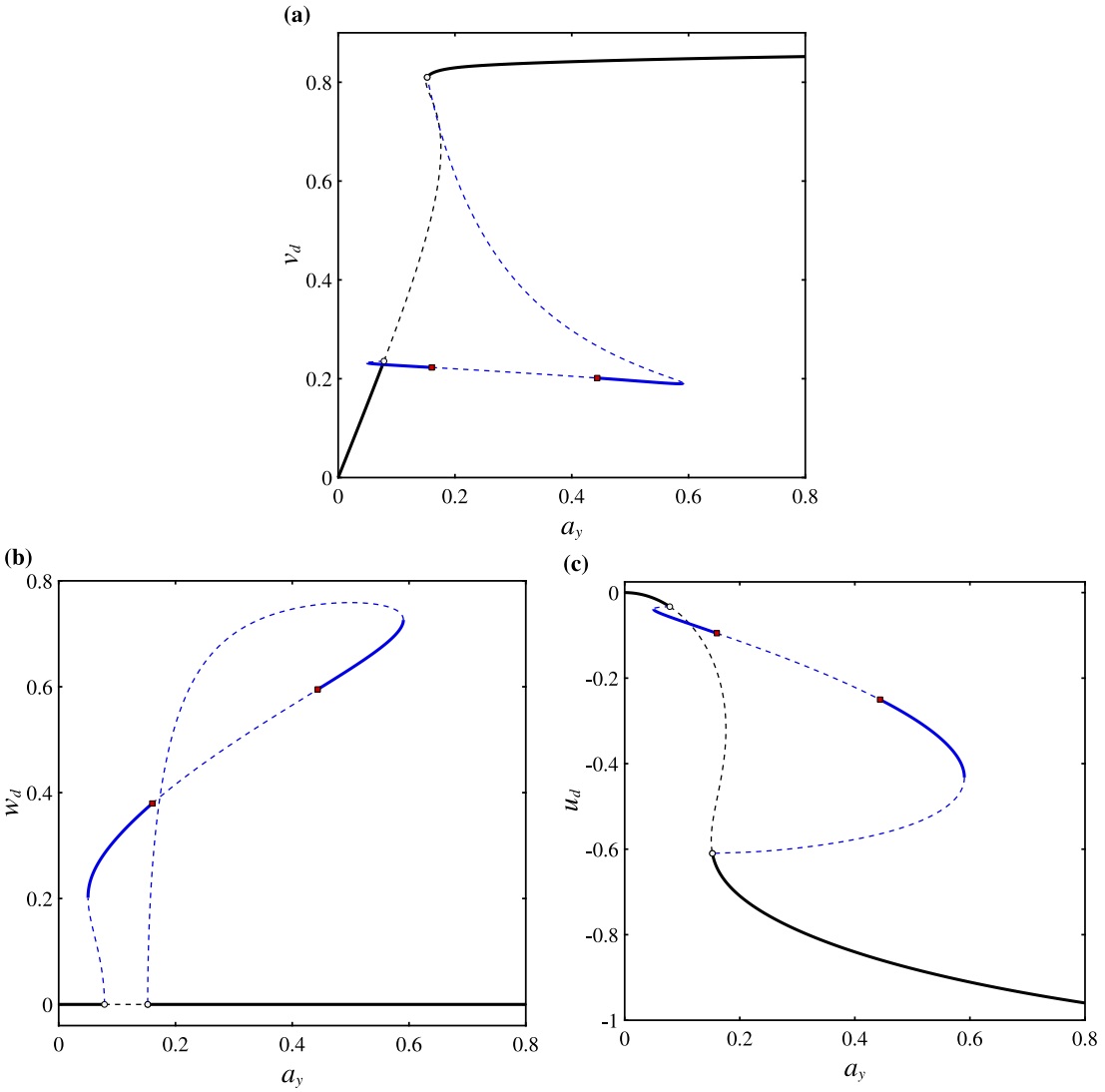

Fig. 10. Base-acceleration-amplitude diagrams of the cantilevered beam showing the tip oscillation amplitudes at $\Omega_y/\omega_1 = 1.02$ for (a, b) transverse motions in the y and z directions, respectively, and (c) longitudinal motion. [▬] Stable periodic solution, [- - -] unstable periodic solution. Squares and circles denote torus bifurcations and branch points, respectively.

y direction if the base-acceleration amplitude is sufficiently small. However, at larger base-acceleration amplitudes, out-of-plane transverse motion branches emerge, resulting in 3D oscillations, even though the excitation is in the y direction.

Fig. 10 shows the maximum oscillation amplitudes of the cantilever at $\Omega_y/\omega_1 = 1.02$ versus the base-acceleration magnitude. The figure shows that as the base acceleration is increased from 0, two bifurcations occur at points denoted by circles (corresponding to $a_y = 0.0784$ and 0.1524), which renders the planar motion unstable and leads to a three-dimensional motion. As shown in Fig. 10(b), new out-of-plane solution branches emerge from these bifurcation points. In the 3D motion region, two saddle–node bifurcations occur at $a_y = 0.0502$ and 0.5903, with two torus bifurcations in between, denoted by squares. To better show the 2D and 3D regions of motion as the base acceleration is increased, Fig. 11 is constructed which illustrates the three-dimensional base-acceleration response of the system of Fig. 10.

The three-dimensional diagram of the maximum amplitudes of the two transverse motions versus the base-acceleration magnitude for various excitation frequency ratios (close to primary resonance) is depicted in Fig. 12. The figure reveals that, the saddle–node bifurcation in the 3D region is shifted to larger base-acceleration magnitudes as the excitation frequency is increased. Furthermore, the unstable periodic region between the two torus bifurcations in the 3D regime becomes narrower as the excitation frequency ratio gets closer to 1, and it completely disappears for the case $\Omega_y/\omega_1 = 1.006$.

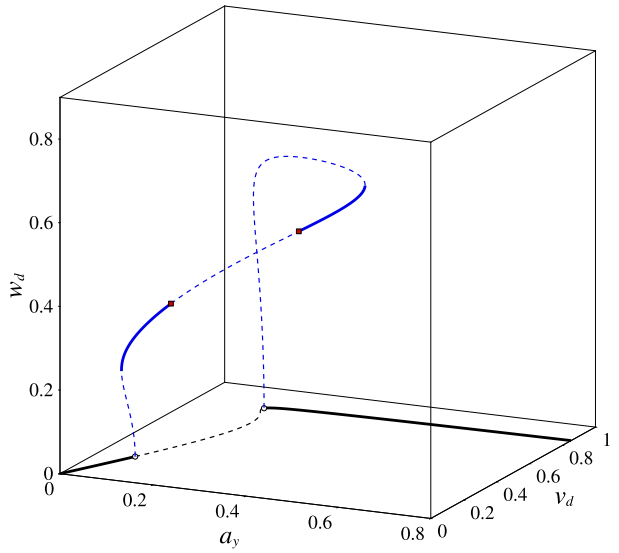

Fig. 11. Three-dimensional base-acceleration-amplitude diagram of the system of Fig. 10 showing regions of 2D and 3D motion. [▬] Stable periodic solution, [- - -] unstable periodic solution. Squares and circles denote torus bifurcations and branch points, respectively.

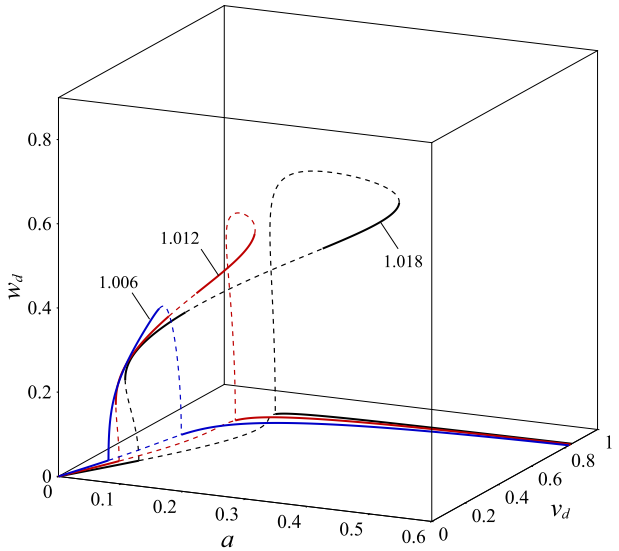

Fig. 12. Three-dimensional base-acceleration-amplitude diagram of the cantilevered beam for various excitation frequency ratios (Ω_y/ω_1). [▬] Stable periodic solution, [- - -] unstable periodic solution.

6. Convergence analysis

In this section, a convergence analysis is conducted to ensure that the employed 18-dof discretised model yields converged results. The results of the convergence analysis are shown in Fig. 13. Three discretised models are constructed, i.e. 3-, 6-, and 18-dof ones, and the primary resonance response is obtained for each case using the same parameters as in the case of Fig. 5. For each discretised model, the same number of modes are considered for ψ, θ, and ϕ. As seen, the 3-dof model does not give reliable predictions near the peak oscillation. The 6-dof model gives more reliable predictions, but the result has not yet converged. The 18-dof model used in this study, on the other hand, gives fully converged results and accurate predictions at any amplitude. It should be noted that the results for a 12-dof discretised model were also obtained but not shown here so that figures are more visible.

7. Comparison to the third-order nonlinear model

In this section, the proposed exact model's predictions are compared to those of the nonlinear third-order model of a cantilever developed by Nayfeh and Pai [43] to examine the limitations of a truncated model. Since the third-order model in Ref. [43] uses a

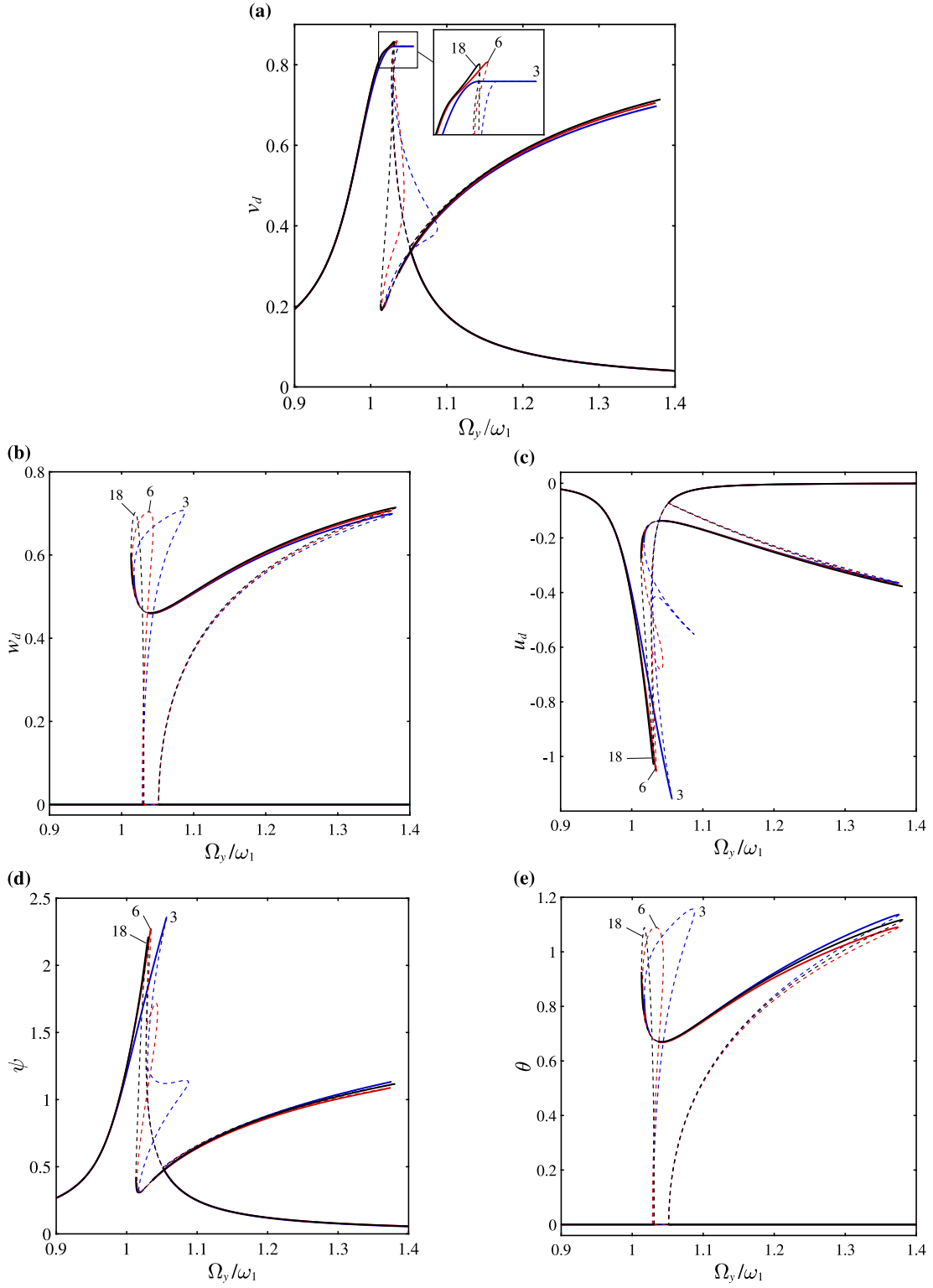

Fig. 13. Convergence analysis of the geometrically exact model, showing the frequency–amplitude diagrams for displacements and rotations based on three discretised models, i.e. a 3-dof, a 6-dof, and an 18-dof model. (a, b) the in-plane and out-of-plane tip transverse displacements, respectively, (c) tip longitudinal displacement, and (d, e) in-plane and out-of-plane rotations, respectively. [▬] Stable periodic solution, [- - -] unstable periodic solution.

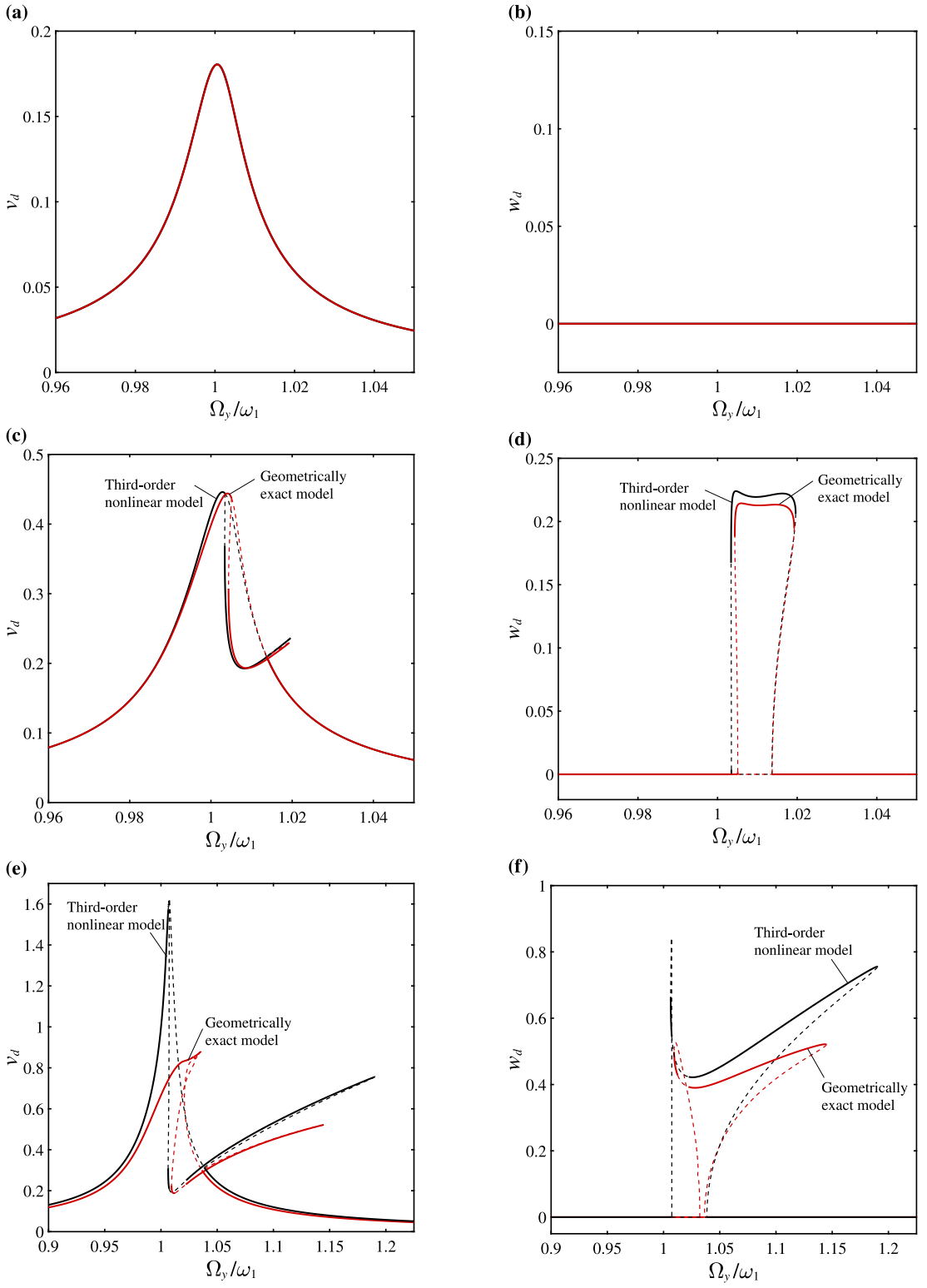

Fig. 14. Comparison between the third-order nonlinear model and the proposed geometrically exact model. The in-plane and out-of-plane transverse motion at (a, b) $a_y = 0.02$, (c, d) $a_y = 0.05$, and (e, f) $a_y = 0.20$. [▬] Stable periodic solution, [- - -] unstable periodic solution.

linear viscous damping model, rather than a viscoelastic formulation, the corresponding terms for a linear viscous damping model are added to the model proposed in this study and the material viscosity is set to zero. For both models, the damping ratio ζ is set to 0.007. The rest of the system parameters are kept the same as those of the case of Fig. 5. Furthermore, 12 degrees of freedom are retained in the discretised of the third-order model, i.e. by retaining 6 modes for each transverse motion, which ensures converged results.

The 3D response of the cantilever in the primary resonance region is examined using the proposed geometrically exact model as well as the third-order nonlinear model. The detailed comparison between the exact and 3rd-order models is shown in Fig. 14. To better illustrate the differences between the two models, the frequency–amplitude diagrams are constructed for three different values of the base acceleration, i.e. $a_y = 0.02$, 0.05, and 0.20. As seen in sub-figures (a, b), at a relatively small base acceleration magnitude of 0.02, the exact and third-order models predict virtually the same results; additionally, for this case, both models predict a 2D motion with the out-of-plane transverse motion amplitude remaining at 0 in the whole primary resonance region. By increasing a_y to 0.05, slight differences between the two model start to appear. For this value of a_y, the third-order nonlinear model still performs well in capturing the response of the cantilever, which is due to the fact that the cantilever oscillation amplitude is not too large. As the base acceleration magnitude is increased to a relatively large value of $a_y = 0.20$, the limitations of the third-order nonlinear model become very visible. As seen, the third-order model predicts a peak amplitude of around 1.6 for v_d which implies a displacement of 160% of the length of the beam, which is impossible. Additionally, there are visible differences between the out-of-plane motion predicted by the third-order model and that obtained by the exact model. Hence, the third-order nonlinear model works well only for relatively small base acceleration magnitudes. As the base acceleration magnitude is increased to relatively large values, the third-order model predictions deviate to wrong values, which signifies the importance of the proposed geometrically exact model. It should be noted that for the case of the third-order model, the geometric nonlinearity tends to generate a hardening-type nonlinear behaviour while the inertial nonlinearity causes a softening-type nonlinear behaviour [48]. When both are considered (which is the case here), the hardening behaviour is almost cancelled out by the softening behaviour, and hence the reason why the third-order model shows a linear-like behaviour in the 2D resonance region.

8. Concluding remarks

This study examined the extremely large-amplitude three-dimensional dynamics of cantilevers based on a new geometrically exact model. To this end, the equations of motion were derived for three Euler angles of the cantilever centreline while keeping all terms exact, which allows for accurate predictions of oscillations of extremely large amplitudes. Utilising the Galerkin method, the discretised equations of motion were obtained while ensuring that all terms are kept intact. The resultant high-dimensional discretised model was solved through use of a continuation technique.

The accuracy of the proposed model for both 2D and 3D cases was verified by comparison to an exact 2D model in the literature and to a 3D nonlinear finite element model, respectively. Additionally, a convergence analysis showed that low-dimensional models do not yield accurate and converged results; the 18-dof model used in this study, on the other hand, ensures converged results even at large base acceleration magnitudes.

The limitations of the third-order 3D nonlinear model was examined by comparing the frequency–amplitude diagrams obtained by the third-order model at different base acceleration magnitudes to those obtained via the proposed geometrically exact model. It was shown that although the third-order model works well for relatively small base accelerations, it loses accuracy as the base acceleration is increased to larger magnitudes.

It was shown that a base excitation in the y direction gives rise to both in-plane and out-of-plane transverse motions, due to presence of one-to-one internal resonances between the in-plane and out-of-plane transverse modes. However, this behaviour is observed only at sufficiently large base-acceleration magnitudes. In other words, for small enough base accelerations, an excitation in the y direction leads to oscillation only in the y direction, while at larger base-acceleration amplitudes, out-of-plane transverse motion branches emerge, resulting in 3D oscillations. Furthermore, it was shown that at relatively large base acceleration magnitudes, the cantilever oscillation amplitude grows so large that the tip of the cantilever bends backwards. Examining the large-amplitude oscillations in the 3D region showed that the tip of the cantilever creates an oval path at excitation frequencies close to the natural frequency, while the path changes to circular at larger excitation frequencies.

CRediT authorship contribution statement

Hamed Farokhi: Conceptualization, Methodology, Software, Validation, Investigation, Writing - original draft, Writing - review & editing, Visualization. **Alper Erturk:** Writing - review & editing.

Declaration of competing interest

The authors declare that they have no known competing financial interests or personal relationships that could have appeared to influence the work reported in this paper.

References

[1] S.L. Minas, M.P. Païdoussis, Dynamics of a shrouded cantilevered pipe subjected to internal and annular flows, J. Sound Vib. 490 (2021) 115729.
[2] C.K. Hirwani, S.K. Panda, Numerical nonlinear frequency analysis of pre-damaged curved layered composite structure using higher-order finite element method, Int. J. Non-Linear Mech. 102 (2018) 14–24.
[3] J.D. MacLean, S.S. Aphale, A modified linear integral resonant controller for suppressing jump-phenomenon and hysteresis in micro-cantilever beam structures, J. Sound Vib. 480 (2020) 115365.
[4] J. Li, X. He, X. Yang, Y. Liu, A consistent geometrically nonlinear model of cantilevered piezoelectric vibration energy harvesters, J. Sound Vib. 486 (2020) 115614.
[5] K. Mehar, S.K. Panda, T.R. Mahapatra, Theoretical and experimental investigation of vibration characteristic of carbon nanotube reinforced polymer composite structure, Int. J. Mech. Sci. 133 (2017) 319–329.
[6] C. Hirwani, T. Mahapatra, S. Panda, S. Sahoo, V. Singh, B. Patle, Nonlinear free vibration analysis of laminated carbon/epoxy curved panels, Defence Sci. J. 67 (2) (2017) 207.
[7] P.V. Katariya, S.K. Panda, Numerical frequency analysis of skew sandwich layered composite shell structures under thermal environment including shear deformation effects, Struct. Eng. Mech. 71 (6) (2019) 657–668.
[8] N. Sharma, T.R. Mahapatra, S.K. Panda, Numerical analysis of acoustic radiation responses of shear deformable laminated composite shell panel in hygrothermal environment, J. Sound Vib. 431 (2018) 346–366.
[9] C.K. Hirwani, S.K. Panda, T.R. Mahapatra, S.S. Mahapatra, Numerical study and experimental validation of dynamic characteristics of delaminated composite flat and curved shallow shell structure, J. Aerosp. Eng. 30 (5) (2017) 04017045.
[10] P.V. Katariya, K. Mehar, S.K. Panda, Nonlinear dynamic responses of layered skew sandwich composite structure and experimental validation, Int. J. Non-Linear Mech. 125 (2020) 103527.
[11] K. Zhou, Q. Ni, W. Chen, H. Dai, P. Hagedorn, L. Wang, Static equilibrium configuration and nonlinear dynamics of slightly curved cantilevered pipe conveying fluid, J. Sound Vib. 490 (2021) 115711.
[12] G.-X. Wang, H. Ding, L.-Q. Chen, Dynamic effect of internal resonance caused by gravity on the nonlinear vibration of vertical cantilever beams, J. Sound Vib. 474 (2020) 115265.
[13] M. Abdullatif, R. Mukherjee, Effect of intermediate support on critical stability of a cantilever with non-conservative loading: Some new results, J. Sound Vib. 485 (2020) 115564.
[14] J. Deng, O. Guasch, L. Zheng, T. Song, Y. Cao, Semi-analytical model of an acoustic black hole piezoelectric bimorph cantilever for energy harvesting, J. Sound Vib. 494 (2021) 115790.
[15] X. Mei, S. Zhou, Z. Yang, T. Kaizuka, K. Nakano, Enhancing energy harvesting in low-frequency rotational motion by a quad-stable energy harvester with time-varying potential wells, Mech. Syst. Signal Process. 148 (2021) 107167.
[16] T.D. Caliskan, D.A. Bruce, M.F. Daqaq, Micro-cantilever sensors for monitoring carbon monoxide concentration in fuel cells, J. Micromech. Microeng. 30 (4) (2020) 045005.
[17] U. Latif, E. Uddin, M. Younis, J. Aslam, Z. Ali, M. Sajid, A. Abdelkefi, Experimental electro-hydrodynamic investigation of flag-based energy harvesting in the wake of inverted C-shape cylinder, Energy 215 (2021) 119195.
[18] S. Mazharmanesh, J. Young, F.-B. Tian, J.C. Lai, Energy harvesting of two inverted piezoelectric flags in tandem, side-by-side and staggered arrangements, Int. J. Heat Fluid Flow 83 (2020) 108589.
[19] O. Ojo, K. Shoele, A. Erturk, Y.-C. Wang, E. Kohtanen, Numerical and experimental investigations of energy harvesting from piezoelectric inverted flags, in: AIAA Scitech 2021 Forum, 2021, p. 1323.
[20] M. Crespo da Silva, C. Glynn, Nonlinear flexural-flexural-torsional dynamics of inextensional beams. I. Equations of motion, J. Struct. Mech. 6 (4) (1978) 437–448.
[21] M. Crespo da Silva, C. Glynn, Nonlinear flexural-flexural-torsional dynamics of inextensional beams. II. Forced motions, J. Struct. Mech. 6 (4) (1978) 449–461.
[22] A.H. Nayfeh, P.F. Pai, Non-linear non-planar parametric responses of an inextensional beam, Int. J. Non-Linear Mech. 24 (2) (1989) 139–158.
[23] P.F. Pai, A.H. Nayfeh, Non-linear non-planar oscillations of a cantilever beam under lateral base excitations, Int. J. Non-Linear Mech. 25 (5) (1990) 455–474.
[24] S.-R. Hsieh, S.W. Shaw, C. Pierre, Normal modes for large amplitude vibration of a cantilever beam, Int. J. Solids Struct. 31 (14) (1994) 1981–2014.
[25] Z. Feng, L. Leal, Symmetries of the amplitude equations of an inextensional beam with internal resonance, J. Appl. Mech. 62 (1) (1995) 235–238.
[26] T. Anderson, A. Nayfeh, B. Balachandran, Experimental verification of the importance of the nonlinear curvature in the response of a cantilever beam, J. Vib. Acoust. 118 (1) (1996) 21–27.
[27] K. Oh, A.H. Nayfeh, Nonlinear combination resonances in cantilever composite plates, Nonlinear Dynam. 11 (2) (1996) 143–169.
[28] N. Herişanu, V. Marinca, Explicit analytical approximation to large-amplitude non-linear oscillations of a uniform cantilever beam carrying an intermediate lumped mass and rotary inertia, Meccanica 45 (6) (2010) 847–855.
[29] H. Farokhi, M.H. Ghayesh, Geometrically exact extreme vibrations of cantilevers, Int. J. Mech. Sci. 168 (2020) 105051.
[30] R. Eshtehardiha, R. Tikani, S. Ziaei-Rad, Experimental and numerical investigation of energy harvesting from double cantilever beams with internal resonance, J. Sound Vib. 500 (2021) 116022.
[31] S.N. Mahmoodi, N. Jalili, M. Ahmadian, Subharmonics analysis of nonlinear flexural vibrations of piezoelectrically actuated microcantilevers, Nonlinear Dynam. 59 (3) (2010) 397–409.
[32] V. Kumar, J.W. Boley, Y. Yang, H. Ekowaluyo, J.K. Miller, G.T.-C. Chiu, J.F. Rhoads, Bifurcation-based mass sensing using piezoelectrically-actuated microcantilevers, Appl. Phys. Lett. 98 (15) (2011) 153510.
[33] M.I. Friswell, S.F. Ali, O. Bilgen, S. Adhikari, A.W. Lees, G. Litak, Non-linear piezoelectric vibration energy harvesting from a vertical cantilever beam with tip mass, J. Intell. Mater. Syst. Struct. 23 (13) (2012) 1505–1521.
[34] H. Liu, C. Lee, T. Kobayashi, C.J. Tay, C. Quan, Piezoelectric MEMS-based wideband energy harvesting systems using a frequency-up-conversion cantilever stopper, Sens. Actuat A: Phys. 186 (2012) 242–248.
[35] S. Leadenham, A. Erturk, Unified nonlinear electroelastic dynamics of a bimorph piezoelectric cantilever for energy harvesting, sensing, and actuation, Nonlinear Dynam. 79 (3) (2015) 1727–1743.
[36] M. Panyam, M.F. Daqaq, Characterizing the effective bandwidth of tri-stable energy harvesters, J. Sound Vib. 386 (2017) 336–358.
[37] M. Lallart, S. Zhou, Z. Yang, L. Yan, K. Li, Y. Chen, Coupling mechanical and electrical nonlinearities: The effect of synchronized discharging on tristable energy harvesters, Appl. Energy 266 (2020) 114516.
[38] E. Carrera, G. Giunta, Refined beam theories based on a unified formulation, Int. J. Appl. Mech. 2 (01) (2010) 117–143.
[39] A. Pagani, E. Carrera, Unified formulation of geometrically nonlinear refined beam theories, Mech. Adv. Mater. Struct. 25 (1) (2018) 15–31.
[40] A. Pagani, R. Augello, E. Carrera, Frequency and mode change in the large deflection and post-buckling of compact and thin-walled beams, J. Sound Vib. 432 (2018) 88–104.

[41] E. Carrera, A. Pagani, R. Azzara, R. Augello, Vibration of metallic and composite shells in geometrical nonlinear equilibrium states, Thin-Walled Struct. 157 (2020) 107131.
[42] E. Carrera, A. Pagani, D. Giusa, R. Augello, Nonlinear analysis of thin-walled beams with highly deformable sections, Int. J. Non-Linear Mech. 128 (2021) 103613.
[43] A.H. Nayfeh, P.F. Pai, Linear and Nonlinear Structural Mechanics, John Wiley & Sons, 2008.
[44] P.F. Pai, A.H. Nayfeh, A fully nonlinear theory of curved and twisted composite rotor blades accounting for warpings and three-dimensional stress effects, Int. J. Solids Struct. 31 (9) (1994) 1309–1340.
[45] C.K. Hirwani, S.K. Panda, T.R. Mahapatra, S.S. Mahapatra, Nonlinear transient finite-element analysis of delaminated composite shallow shell panels, AIAA J. 55 (5) (2017) 1734–1748.
[46] M.C. Kunche, P.K. Mishra, H.B. Nallala, C.K. Hirwani, P.V. Katariya, S. Panda, S.K. Panda, Theoretical and experimental modal responses of adhesive bonded T-joints, Wind Struct. 29 (5) (2019) 361–369.
[47] S. Timoshenko, J. Goodier, Analysis of stress and strain in three dimensions, in: Theory of Elasticity, 3rd ed., McGraw-Hill, New York, 1970, pp. 13–313.
[48] H. Farokhi, M.H. Ghayesh, S. Hussain, Large-amplitude dynamical behaviour of microcantilevers, Internat. J. Engrg. Sci. 106 (2016) 29–41.